Available online at www.sciencedirect.com
ScienceDirect
Journal of Sound and Vibration 309 (2008) 86–95
JOURNAL OF SOUND AND VIBRATION
www.elsevier.com/locate/jsvi

Vibration analysis of a new curved beam element

Z.H. Zhu[a], S.A. Meguid[b,*,1]

[a]Department of Earth and Space Science and Engineering, York University 4700 Keele Street, Toronto, Ontario, Canada M3J 1P3
[b]Engineering Mechanics and Design Laboratory, Department of Mechanical and Industrial Engineering, University of Toronto, 5 King's College Road, Toronto, Ontario, Canada M5S 7G8

Received 1 August 2005; received in revised form 28 March 2007; accepted 18 April 2007

Abstract

The common practice in developing a locking-free curved beam element is to ensure that its interpolation functions of displacement explicitly satisfy the inextensible bending mode condition for the membrane locking-free instead of the rigid body modes. In this paper, we study the impact of this practice on the dynamic characteristics of a finite element by conducting vibration analysis using our newly developed three-node locking-free curved beam element. In this case, the inextensible bending mode condition is satisfied explicitly, while the rigid body modes are satisfied implicitly to 4th-order accuracy. Numerical and experimental examples show that with the newly developed curved beam element, developed by using the implicit representation of a rigid body mode condition, it is possible to recover the rigid body modes of curved beams with low and medium slenderness ratios. This is even true for cases involving a half-circular element and the vibration of the curved beam is predicted with high accuracy.

1. Introduction

Curved beam elements, which are based on the curvilinear strain field description, outperform their straight counterparts in modeling curved beams with higher accuracy by coarse meshes. However, the formulation of curved beams is not a simple extension of the straight beam formulations because of the membrane-locking problem. This phenomenon was initially attributed to the inability of low-order polynomial displacement interpolation functions to represent the rigid body modes of the curved element properly [1]. The requirement for the terms of rigid body modes in the displacement interpolation functions leads to the addition of trigonometric terms to the coupled polynomial displacement interpolation functions which yielded better results [1,2]. Unfortunately, the trigonometric terms will become trivial as the curved beam's curvature approaches zero. The degenerated displacement interpolation functions are insufficient to represent the bending deformation of the straightened beam. To overcome the limitation of the trigonometric terms, alternative studies [3,4] showed that adopting higher order polynomial displacement interpolation functions, without including the terms of rigid body modes explicitly, would alleviate the membrane locking. Stolarski

*Corresponding author. Tel.: +1 416 9785741; fax: +1 416 9787753.
E-mail address: meguid@mie.utoronto.ca (S.A. Meguid).
[1]Presently, Head, Aerospace Engineering Division, MAE, Nanyang Technological University, Singapore.

0022-460X/$ - see front matter © 2007 Elsevier Ltd. All rights reserved.
doi:10.1016/j.jsv.2007.04.051

and Belytschko [5] and Prathap and Bhashyam [6] further identified the cause of the locking as the failure of the independently interpolated displacement functions to recover correct constraints from the membrane strains in the state of inextensible bending and not because those displacement functions did not contain the rigid body modes explicitly. Reduced integration of membrane strain energy was proposed to improve the behavior of the curved beam element. In addition, Prathap and Babu [7] and Balasubramanian and Prathap [8] proposed a field consistency interpolation method, in which the axial displacement function is required to be one order higher than the transverse displacement function. Among the curved beam element formulations, the field consistency concept is the most appealing since it allows predicting a priori any poor convergence due to the locking. Detailed reviews of curved element formulations can be found in the works of Raveendranath et al. [9–11] and Bucalem and Bathe [12]. To improve the computational efficiency further, while being able to recover the inextensible bending mode of curved beams, Raveendranath et al. [9] proposed a brilliant approach to derive the lower order, field consistent, polynomial displacement interpolation functions for curved beam elements by coupling the axial and transverse displacement interpolation functions through the equilibrium equations. Recently, Zhu and Meguid [13,14] extended the coupled field consistency interpolation method into the geometrically nonlinear curved beam analysis by proposing a three-node, three-dimensional curved beam element. The polynomial displacement interpolation functions are derived by coupling the axial and transverse displacement fields with presumably linear membrane and torsional strain fields in order to avoid the mathematical complexity of the equilibrium equations in case of large displacements and rotations. However, all the above works focused on the recovery of the inextensible bending mode, which is the membrane locking-free of the curved beam element. The effects of not including the rigid body modes explicitly in the displacement interpolation functions on the vibration and dynamic characteristics of the derived curved beam elements are not investigated thoroughly. By satisfying the inextensible bending mode explicitly instead of the rigid body modes, the polynomial interpolation functions of the curved beam elements [7–11,13,14] will give the correct rigid body modes only in the limit of zero length of the element. This is referred to as the implicit representation of rigid body modes [15]. In order to ensure the convergence of the derived curved beam element in the vibration and dynamic analyses, we will examine the implicit representation of the rigid body modes used in our earlier curved beam element formulations [14] for its accuracy and efficiency in recovering the rigid body modes, predicting the natural frequencies and analyzing the vibrations of the curved structures.

This paper consists of four sections. Following this introduction, a brief summary of the theoretical development of curved beam element is provided in Section 2. In Section 3, we discuses the accuracy of the implicit representation of rigid body modes. In Section 4, we demonstrate the capability of the curved beam element in recovering the rigid body modes, the convergence characteristic of the element in predicting the natural frequencies by comparison with existing theoretical results, and the accuracy of the element in dynamic analysis by experimental work using a free vibrating cantilever beam and high-speed imaging technique. In Section 5, we conclude the paper.

2. Finite element formulation of curved beam element

Consider a three-dimensional curved beam element shown in Fig. 1. The geometry of the element is described by its length ${}^tL$, curvature ${}^t\kappa$, and nodal coordinates $(X_i,\ Y_i,\ Z_i)$ in the global Cartesian coordinate system $OXYZ$. Local curvilinear coordinates x, y and z are defined with the z-axis along the neutral axis of the beam, the x-axis in the normal direction and the y-axis in the bi-normal direction.

In the follow sections, the preceding superscript/subscript t notations are used to represent the time status of a variable: ${}_t()$ denotes the time increment of a variable with respect to time t; ${}^t()$ denotes the variable at time t; ${}_t^{t+\Delta t}()$ denotes the variable at time $t+\Delta t$ with respect to time t, respectively.

The incremental Green–Lagrange strains of the curved beam at time $t+\Delta t$ are defined with respect to time t [14], such as

$$ {}_tE_{33} = {}_t\varepsilon - x_1({}_t\omega_2 - 2{}^t\kappa_t\varepsilon) + x_2{}_t\omega_1, \quad {}_tE_{13} = \frac{x_2}{2}{}_t\eta, \quad {}_tE_{23} = \frac{x_1}{2}{}_t\eta, \tag{1} $$

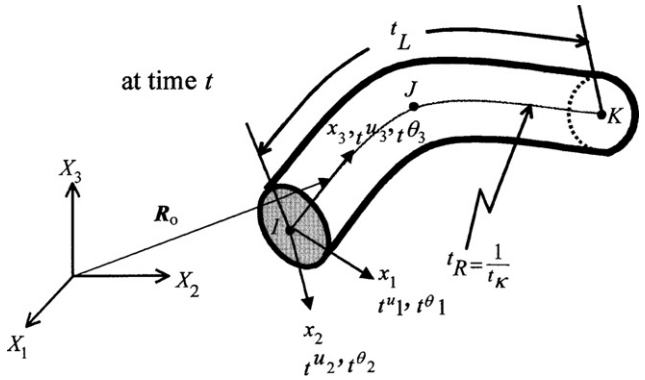

Fig. 1. Geometry of a general spatial curved beam element.

where ${}_t\varepsilon$, ${}_t\omega_1$, ${}_t\omega_2$, ${}_t\eta$ are the incremental membrane strain and curvature rates of the neutral axis and can be expressed in terms of the displacements (${}_tu_i$) and rotations (${}_t\theta_i$)of the neutral axis, such that,

$$ {}_t\varepsilon = {}_tu_{3,3} - {}^t\kappa_t u_1 + 1/2\left[\underline{({}_tu_{1,3} + {}^t\kappa_t u_1)^2 + ({}_tu_{2,3})^2 + ({}_tu_{3,3} - {}^t\kappa_t u_1)^2}\right], \tag{2a} $$

$$ {}_t\omega_1 = -{}_tu_{2,33} + {}^t\kappa_t\theta_3 \underline{+{}_t\theta_3({}_tu_{1,33} + 2{}^t\kappa_t u_{3,3} - {}^t\kappa^2{}_tu_1) + {}_tu_{2,3}({}_tu_{3,33} - 2{}^t\kappa_t u_{1,3} - {}^t\kappa^2{}_tu_3)}, \tag{2b} $$

$$ {}_t\omega_2 = -{}_tu_{1,33} + {}^t\kappa_t u_{3,3} \underline{+{}_t\theta_3{}_tu_{2,33} - ({}_tu_{1,3} - {}^t\kappa_t u_3)({}_tu_{3,33} - 2{}^t\kappa_t u_{1,3} - {}^t\kappa^2{}_tu_3)}, \tag{2c} $$

$$ {}_t\eta = -{}_t\theta_{3,3} + {}^t\kappa_t u_{2,3} + \underline{{}^t\kappa_t\theta_3({}_tu_{1,3} + {}^t\kappa_t u_3) + {}_tu_{2,3}({}_tu_{1,33} + {}^t\kappa_t u_{3,3})}. \tag{2d} $$

The underlined terms in the above expressions are the nonlinear parts of the incremental membrane strain and curvature rates of the neutral axis due to the large displacements and rotations. Assume the displacement interpolations for the three-node curved beam element as

$$ {}_tu_1 = a_0 + a_1x_3 + a_2x_3^2 + a_3x_3^3 + a_4x_3^4 + a_5x_3^5, \tag{3a} $$

$$ {}_tu_2 = b_0 + b_1x_3 + b_2x_3^2 + b_3x_3^3 + b_4x_3^4 + b_5x_3^5, \tag{3b} $$

$$ {}_tu_3 = a_6 + a_7x_3 + a_8x_3^2 + \frac{{}^t\kappa}{3}a_2x_3^3 + \frac{{}^t\kappa}{4}a_3x_3^4 + \frac{{}^t\kappa}{5}a_4x_3^5 + \frac{{}^t\kappa}{6}a_5x_3^6, \tag{3c} $$

$$ {}_t\theta_1 = -b_1 - 2b_2x_3 - 3b_3x_3^2 - 4b_4x_3^3 - 5b_5x_3^4, \tag{3d} $$

$$ {}_t\theta_2 = (a_1 + {}^t\kappa a_6) + (2a_2 + {}^t\kappa a_7)x_3 + (3a_3 + {}^t\kappa a_8)x_3^2 + \left(4a_4 + \frac{{}^t\kappa^2}{3}a_2\right)x_3^3 + \left(5a_5 + \frac{{}^t\kappa^2}{4}a_3\right)x_3^4 + \frac{{}^t\kappa^2}{5}a_4x_3^5 + \frac{{}^t\kappa^2}{6}a_5x_3^6, \tag{3e} $$

$$ {}_t\theta_3 = b_6 + b_7x_3 + b_8x_3^2 - {}^t\kappa b_3x_3^3 - {}^t\kappa b_4x_3^4 - \kappa b_5x_3^5, \tag{3f} $$

where a_i and b_i are the coefficients of the interpolation functions, and ${}^t\kappa$ is the curvature of the curved beam element. Obviously, the above displacement interpolation functions will decouple and reduce to the shape functions for the three-node straight beam element as the curvature ${}^t\kappa$ approaches zero.

By substituting the expressions for displacement ${}_tu_1$ and ${}_tu_3$ (Eqs. (3a) and (3b)) into Eq. (2a) and ignoring the higher order terms, the inextensible bending condition can be written as

$$ {}_t\varepsilon \approx a_7 - {}^t\kappa a_0 + (2a_8 - {}^t\kappa a_1)x_3 = 0 $$

or

$$a_7 - {}^t\kappa a_0 = 0 \quad \text{and} \quad 2a_8 - {}^t\kappa a_1 = 0. \tag{4}$$

From Eq. (4) it can be seen that there are no spurious terms in the constraint equations since each constraint equation contains the contributions from the axial and transverse displacement fields. Thus, by using the proposed displacement fields it is possible to recover the inextensible bending mode of the curved beam element, which ensures that the proposed interpolations are free from the membrane locking.

The incremental principle of virtual work at time $t+\Delta t$ with respect to the reference configuration at time t in the Updated Lagrangian description can be written as

$$\int_{t_L} \left[\delta({}^tU) + \delta({}^tW_{\text{int}}) + \delta({}^tW_{\text{inert}}) + \delta({}^tW_{\text{ext}})\right] \mathrm{d}x_3 = 0, \tag{5}$$

where

$$\delta({}^tU) = {}_tE^tA_t\varepsilon\delta({}_t\varepsilon) + \sum_{i=1}^{2} {}_tE^tI_{it}\omega_i\delta({}_t\omega_i) + {}_tG^tJ_t\eta\delta({}_t\eta),$$

$$\delta({}^tW_{\text{int}}) = {}^tT\delta({}_t\varepsilon) + \sum_{i=1}^{2} {}^tM_i\delta({}_t\omega_i) + {}^tM_3\delta({}_t\eta),$$

$$\delta({}^tW_{\text{inert}}) = {}^{t+\Delta t}\rho\left({}^{t+\Delta t}A\sum_{i=1}^{3} {}^{t+\Delta t}\ddot{u}_i\delta({}_tu_i) + \sum_{i=1}^{2} {}^{t+\Delta t}I_{it}\ddot{\theta}_i\delta({}_t\theta_i) + {}^{t+\Delta t}J_t\ddot{\theta}_3\delta({}_t\theta_3)\right),$$

$$\delta({}^tW_{\text{ext}}) = -\sum_{i=1}^{3} {}^{t+\Delta t}f_i\delta({}_tu_i),$$

and δ is the variational operator, ${}_tE$ and ${}_tG$ are the tangent Young's and shear modulus, ${}^tA$ is the area of cross section, ${}^tI_i$ ($i = 1,2$) and ${}^tJ$ are the moments of inertia and the polar moment of inertia of cross section, ${}^tT$ is the tension, ${}^tM_i$ ($i = 1,2,3$) are the bending and torsional moments, ${}^{t+\Delta t}\rho$ is the material density and ${}^{t+\Delta t}f_i$ is the distributed force along the beam, respectively.

By substituting Eqs. (2)–(3) into Eq. (5), we derive the discretized finite element equation of motion of the curved beam element,

$$[{}^t_t\mathbf{M}]\{{}_t\ddot{\mathbf{u}}\} + [{}^t_t\mathbf{C}]\{{}_t\dot{\mathbf{u}}\} + [{}^t_t\mathbf{K}]\{{}_t\mathbf{u}\} = \{{}^{t+\Delta t}\mathbf{F}\} - \{{}^t\mathbf{F}_S\} - \{{}^t\mathbf{F}_I\}, \tag{6}$$

where $[{}^t_t\mathbf{M}]$, $[{}^t_t\mathbf{C}]$, $[{}^t_t\mathbf{K}]$ are the mass, damping and stiffness matrices, $\{{}_t\ddot{\mathbf{u}}\}$, $\{{}_t\dot{\mathbf{u}}\}$, $\{{}_t\mathbf{u}\}$ are, respectively, the acceleration, velocity and displacement vectors, and $\{{}^{t+\Delta t}\mathbf{F}\}$, $\{{}^t\mathbf{F}_S\}$, $\{{}^t\mathbf{F}_I\}$ are the external, initial stress, and inertia load vectors, respectively. The damping matrix is the Rayleigh damping matrix [16], so

$$[{}^t_t\mathbf{C}] = \alpha_v[{}^t_t\mathbf{M}] + \beta_v[{}^t_t\mathbf{K}], \quad \alpha_v = \frac{4\pi f_1 f_2(f_2\xi_1 - f_1\xi_2)}{f_2^2 - f_1^2}, \quad \beta_v = \frac{f_2\xi_2 - f_1\xi_1}{\pi(f_2^2 - f_1^2)}, \tag{7}$$

where α_v and β_v are the Rayleigh damping coefficients, f_1 and f_2 are the lower and upper bound frequencies of interest in Hz, and ξ_1 and ξ_2 are the corresponding critical damping ratios, respectively.

3. Accuracy of implicit representation of rigid body modes

The accuracy of the implicit representation of rigid body modes of the displacement interpolations for the three-node curved beam element in Eq. (3) is examined by using the polynomial approximation of the rigid body modes. The six rigid body modes of the curved beam element in space can be expressed as

(i) in-plane translation modes:

$$\begin{aligned} {}^tu_1 &= c_1\ \cos({}^t\kappa x_3) + c_2\ \sin({}^t\kappa x_3), \\ {}^tu_3 &= c_1\ \sin({}^t\kappa x_3) - c_2\ \cos({}^t\kappa x_3), \end{aligned} \tag{8a}$$

(ii) out-of-plane translation mode

$$ {}^{t}u_2 = c_3, \tag{8b} $$

(iii) in-plane rotation

$$ {}^{t}u_3 = c_6, \tag{8c} $$

(iv) (iv) out-of-plane rotation

$$ \begin{aligned} {}^{t}u_2 &= c_4\ \sin({}^{t}\kappa x_3) + c_5\ \cos({}^{t}\kappa x_3), \\ {}^{t}\theta_1 &= -c_4{}^{t}\kappa\ \cos({}^{t}\kappa x_3) + c_5^{t}\kappa\ \sin({}^{t}\kappa x_3), \\ {}^{t}\theta_3 &= -c_4^{t}\kappa\ \sin({}^{t}\kappa x_3) - c_5\,{}^{t}\kappa\ \cos({}^{t}\kappa x_3), \end{aligned} \tag{8d} $$

where c_i $(i = 1,2,\ldots 6)$ are the constants representing the rigid body modes of the six degrees of freedom.

Substituting Eq. (8) into Eq. (2) will generate zero strains, i.e., they are rigid body modes. By expanding and approximating the trigonometric terms in Eq. (8) with the elemental interpolation functions in Eq. (3), we obtain

$$ {}^{t}u_1 \approx c_1\left[1 - \frac{1}{2}({}^{t}\kappa x_3)^2 + \frac{1}{24}({}^{t}\kappa x_3)^4\right] + c_2\left[({}^{t}\kappa x_3) - \frac{1}{6}({}^{t}\kappa x_3)^3 + \frac{1}{120}({}^{t}\kappa x_3)^5\right], \tag{9a} $$

$$ {}^{t}u_2 \approx c_3 + c_4\left[({}^{t}\kappa x_3) - \frac{1}{6}({}^{t}\kappa x_3)^3 + \frac{1}{120}({}^{t}\kappa x_3)^5\right] + c_5\left[1 - \frac{1}{2}({}^{t}\kappa x_3)^2 + \frac{1}{24}({}^{t}\kappa x_3)^4\right], \tag{9b} $$

$$ {}^{t}u_3 \approx c_1\left[({}^{t}\kappa x_3) - \frac{1}{6}({}^{t}\kappa x_3)^3 + \frac{1}{120}({}^{t}\kappa x_3)^5\right] - c_2\left[1 - \frac{1}{2}({}^{t}\kappa x_3)^2 + \frac{1}{24}({}^{t}\kappa x_3)^4 - \frac{1}{720}({}^{t}\kappa x_3)^6\right] + c_6, \tag{9c} $$

$$ {}^{t}\theta_1 \approx -c_4{}^{t}\kappa\left[1 - \frac{1}{2}({}^{t}\kappa x_3)^2 + \frac{1}{24}({}^{t}\kappa x_3)^4\right] + c_5^{t}\kappa\left[({}^{t}\kappa x_3) - \frac{1}{6}({}^{t}\kappa x_3)^3\right], \tag{9d} $$

$$ {}^{t}\theta_2 = 0, \tag{9e} $$

$$ {}^{t}\theta_3 \approx -c_4{}^{t}\kappa\left[({}^{t}\kappa x_3) - \frac{1}{6}({}^{t}\kappa x_3)^3 + \frac{1}{120}({}^{t}\kappa x_3)^5\right] - c_5^{t}\kappa\left[1 - \frac{1}{2}({}^{t}\kappa x_3)^2 + \frac{1}{24}({}^{t}\kappa x_3)^4\right]. \tag{9f} $$

Eq. (9) is the best approximation of the rigid body modes that can be represented by the displacement interpolation functions given in Eq. (3) for the three-node curved beam element.

Substituting Eq. (9) into the linear portion of the membrane strain and curvature changes in Eq. (2) leads to

$$ {}_{t}\varepsilon = {}_{t}\eta = 0, $$

$$ {}_{t}\omega_1 = -c_4\frac{({}^{t}\kappa)^2}{120}({}^{t}\beta)^5 - c_5\frac{({}^{t}\kappa)^2}{24}({}^{t}\beta)^4, \quad {}_{t}\omega_2 = c_1\frac{({}^{t}\kappa)^2}{24}({}^{t}\beta)^4 + c_2\frac{({}^{t}\kappa)^2}{120}({}^{t}\beta)^5, \tag{10} $$

where $({}^{t}\beta) = {}^{t}\kappa^{t}L$ is the angle subtended by the element. Eq. (10) shows that the approximation of rigid body modes gives zero membrane and torsional strain but non-zero bending strain. For instance, the approximation of translational displacement causes zero membrane strain but non-zero bending strain. The corresponding non-zero bending strain energy is

$$ {}^{t}U = \{c_2, c_1, c_4, c_5\}^{\mathrm{T}}\begin{bmatrix} {}^{t}\mathbf{Ki} & 0 \\ 0 & {}^{t}\mathbf{Ki} \end{bmatrix}\begin{Bmatrix} c_2 \\ c_1 \\ c_4 \\ c_5 \end{Bmatrix}, \quad {}^{t}\mathbf{Ki} = \frac{{}_{t}E^{t}I_i({}^{t}\kappa)^3({}^{t}\beta)^9}{2851200}\begin{bmatrix} 18({}^{t}\beta)^2 & 99({}^{t}\beta) \\ 99({}^{t}\beta) & 550 \end{bmatrix}. \tag{11} $$

As the element size decreases, the subtended angle (${}^t\beta$) decreases. Consequently the non-zero bending strain energy in Eq. (11) caused by the implicit representation approaches zero at the rate of 9th order as the length of the beam approaches zero. Therefore, the displacement interpolation functions of the curved beam element satisfy the implicit representation of the rigid body modes. The higher the order of the interpolation functions of the element, the less the error in recovering the rigid body mode and the faster the convergence to the correct rigid body modes as the element length approaches to zero. Finally, from Eq. (11) it can also be seen that the interpolation functions of displacement in Eq. (3) will give the correct rigid body modes as the curvature of the element approaches zero.

4. Numerical examples

4.1. Recovery of rigid Body modes of free circular arc

Consider the vibration of a free circular arc. Let its shape vary from a half-circular arc to a straight beam. The corresponding angle β subtended by the arc ranges from π to zero. The frequencies of the first seven modes are calculated by using our newly developed element. Theoretically, the six lowest modes of the free arc should be rigid body modes with zero frequency. As expected from Eq. (11), the new element recovers all six rigid body modes for the straightened beam ($\beta = 0$ and $\kappa = 0$). For $\beta = \pi/4$, the new element recovers five zero frequency modes accurately. The sixth zero frequency mode is recovered approximately. As the subtended angle β increases to π, only two zero frequency modes are recovered accurately and the rest four zero frequency modes are recovered approximately. Shown in Fig. 2 are the results of approximately recovered zero frequency modes as a function of the slenderness ratio L/d of the arc, where L and d are the length and the depth of the arc cross-section. All the results are normalized by the frequency of the lowest mode of non-rigid body modes (7th mode). It is found that the implicit representation is accurate at low to moderate values of the slenderness ratio ($L/d \leqslant 100$). For instance, the maximum error margin is less than 0.5% for $\beta = \pi/4$, 1.7% for $\beta = \pi/2$, and 2.8% for $\beta = \pi$ compared with the frequency of the lowest mode of non-rigid body mode. At $L/d \leqslant 10^5$, the maximum error margin is less than 17% for $\beta = \pi/4$, 16% for $\beta = \pi/2$, and 25% for $\beta = \pi$. Although the accuracy of the rigid body modes recovered when the beam is extremely thin is not good, the results in the following example will demonstrate that even in this case there is no significant error in predicting the natural frequencies of the non-rigid body modes

4.2. Convergence and locking check

In the second example we examine the convergence and anti-membrane locking characteristics of the newly developed element in predicting the natural frequencies of curved structures. Consider the free vibration of a

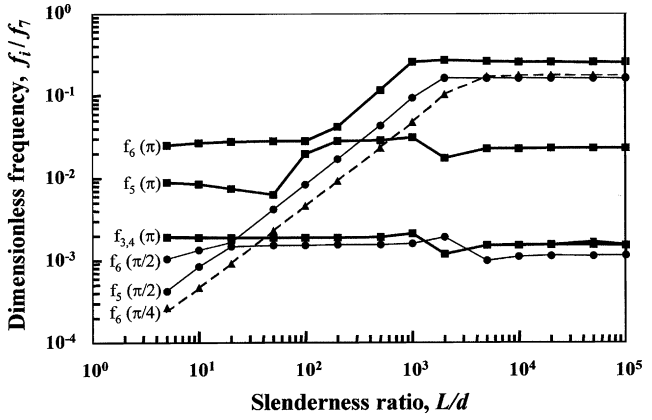

Fig. 2. Recovery of rigid body modes using one new curved beam element. —■— half circular, —●— quarter circular, and ---▲--- one eighth circular.

full circular ring. The vibration of the circular ring can be divided into four modes: flexural in-plane, flexural out-of-plane, axial extensional and torsional vibrations. The fundamental frequencies of the extensional and torsional vibrations are much higher than the inextensible flexural vibration. In order to compare our work with an existing theoretical solution [17], the rotation inertia is neglected but the rotary inertia associated with the beam twisting about its own axis is included. In Table 1 are shown the non-dimensional natural frequencies ($\Omega_i = 2\pi f_i R^2/(EI/\rho A)^{1/2}$) of the first three modes of the extensional, torsional, in-plane and out-of-plane vibrations. The extensional and torsional modes converge with only two elements. With 10 new elements, the flexural modes converge with a maximum discrepancy less than 0.1%. Next, the natural frequencies of flexural in-plane modes are calculated as a function of different slenderness ratios of the ring ranging from moderately thick to extremely thin. Shown in Fig. 3 are the different frequencies of the flexural in-plane modes as a function of slenderness ratio predicted by using the newly developed curved beam element, a tetrahedral solid p-element and thin beam theory. The thin beam theory neglects the effect of the rotation inertia of the beam and its prediction of natural frequencies of flexural modes is independent of the slenderness ratio (the solutions from thin beam theory are shown as flat dotted-lines in Fig. 3). However, the predictions of the solid element theory show that the effect of the rotation inertia of beam is no longer negligible for a moderately thick beam ($L/d \leqslant 40$). The natural frequencies of the flexural modes decrease as the slenderness ratio decreases. The higher the natural frequency, the more significant the effect of the rotation

Table 1
Non-dimensional natural frequencies of a full circular ring

Element no.	Extension	Torsion	In-plane bending			Out-of-plane bending		
	Mode 1	Mode 1	Mode 1	Mode 2	Mode 3	Mode 1	Mode 2	Mode 3
2	200.001	141.421	2.956	12.278		2.773	8.665	
3	200.001	141.421	2.699	8.020	16.763	2.688	7.785	16.323
4	200.000	141.421	2.683	7.681	15.203	2.640	7.617	14.845
5	200.000	141.421	2.683	7.595	14.736	2.621	7.573	14.627
6	200.000	141.421	2.683	7.590	14.587	2.614	7.528	14.573
7	200.000	141.421	2.683	7.590	14.558	2.610	7.506	14.518
8	200.000	141.421	2.683	7.589	14.556	2.609	7.495	14.482
9	200.000	141.421	2.683	7.589	14.553	2.608	7.489	14.461
10	200.000	141.421	2.683	7.589	14.552	2.607	7.485	14.449
Theory [17]	200.000	141.421	2.683	7.589	14.552	2.606	7.478	14.425

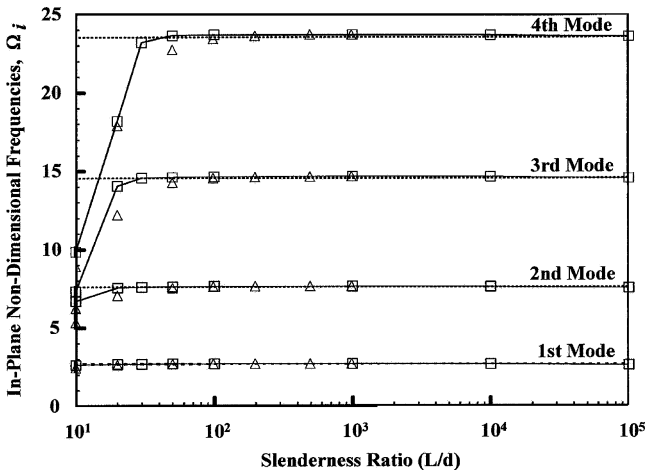

Fig. 3. Natural frequencies of the flexural in-plane modes of a full circular ring: - - - - - - - theory [17], —□— new curved beam element, and △ tetrahedral solid p-element.

inertia. The newly developed curved beam element is based on a thin beam assumption, but includes the effect of the rotational inertia. It is shown that the predictions of the newly developed curved beam element agree exactly with the theoretical solution for a thin beam in cases ranging from extreme slenderness ratios ($L/d \leqslant 10^5$) to the moderate thick region ($L/d = 40$) without any locking. In the region of low slenderness ratios ($L/d \leqslant 40$), the predictions of the newly developed curved beam element are in good agreement with the predictions from solid elements without any locking. The small discrepancy between the new curved beam element and the solid element is due to the shear deformation of the cross-section of beam and not due to the membrane locking. The results shown in Table 1 and Fig. 3 also indicate that the error in recovering the rigid body modes caused by the implicit representation does not affect the prediction accuracy of the frequencies of the non-rigid body modes.

4.3. Experimental validation—Free vibration of a cantilever beam

Consider the cantilever beam shown in Fig. 4. The parameters of the selected test beam are:

Length, $L = 1150\,\text{mm}$; cross-section area, $A = 25.19\,\text{mm}^2$; Moment of inertia, $I = 96.86\,\text{mm}^4$; polar moment of inertia, $J = 193.72\,\text{mm}^4$; young's modulus, $E = 2900\,\text{Mpa}$; and density, $\rho = 1.25 \times 10^{-6}\,\text{kg/mm}^3$. The beam was initially bent by a point load applied laterally at its free end. The load was then suddenly released and the beam was allowed to vibrate freely. The free vibration of the by beam was captured by using a high-speed digital camera at every 1/125 s. The camera resolution was set to 480×420 pixels and the image data were sent to a computer for post-processing. The measured beam length on the image plane was 366 pixels. Thus, the image resolution is $1150/366 = 3.14\,\text{mm/pixel}$. The error margin of the image measurement is ± 0.5 pixels. Hence, the accuracy of the experiment measurement is $\pm 1.57\,\text{mm}$. The experimental measurements captured from the motion images are shown in Figs. 5 and 6. Shown in Fig. 5 are the successive positions of the beam, showing that the beam experienced large displacement and rotation. Shown in Fig. 6 are the measured time histories of the tip displacements of the beam in the axial and transverse directions, From the experimental data in Fig. 6 it can be seen that the frequency of the vibrating beam is 1.25 Hz, which is very close to the theoretical prediction of 1.26 Hz for this cantilever beam [16]. By using logarithmic decrement on the data in Fig. 6 the damping ratio was estimated to be 3.8% [16].

The finite element analysis of the beam was earned out by using four newly developed curved beam elements. The equation of motion in Eq. (6) was solved numerically by the Predictor–Corrector method using the Newmark time stepping scheme with Newton–Raphson iteration [18]. The parameters for time integration, such as the time step, the spectral radius of numerical damping and Rayleigh damping coefficients, were chosen carefully by examining the dynamic characteristics of the vibrating beam. From the experimental data (Fig. 6) the lowest natural frequency of the vibrating beam is close to 1.25 Hz with a damping ratio of 3.8%.

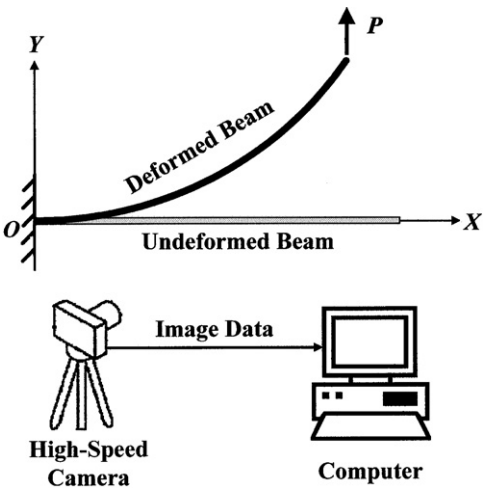

Fig. 4. Scheme of experimental setup.

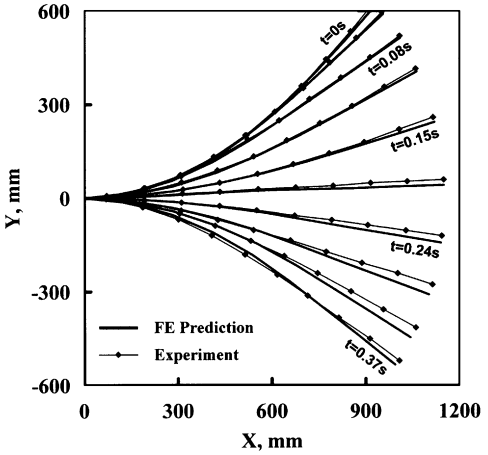

Fig. 5. Comparison of measured and predicted beam positions: —— finite element prediction, and —◆— experimental measurement.

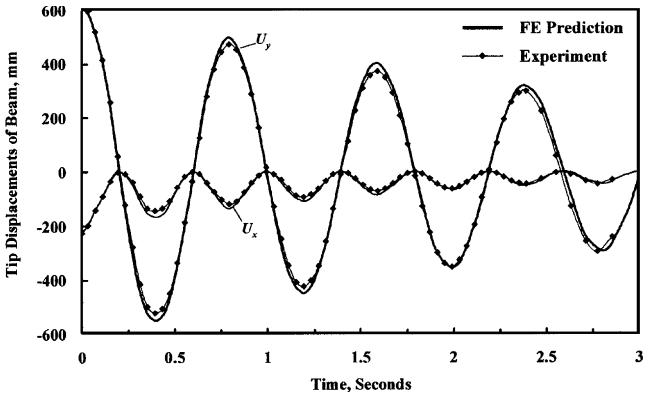

Fig. 6. Time history of tip displacement of beam; —— finite element prediction, and —◆— experimental measurement.

The highest natural frequency of the beam that can be calculated by using the finite element model, which is limited because of the discretization, is 842.5 Hz and this is the frequency of the membrane mode. The membrane damping is usually low and is assumed as 1.0% of critical damping. By substituting the above upper and lower frequencies and the corresponding damping ratios into Eq. (7), we obtain the Rayleigh damping coefficients to be $a_v \approx 0.6$ and $\beta_v \approx 10^{-5}$ over the frequency range from 1.25 to 842.5 Hz. In addition, the work by Kuhl and Crisfield [19] demonstrated that the Newmark integration scheme with the spectral radius $\rho_\infty = 1.0$ is sometime unstable in the nonlinear elastodynamic problem. A lower value of the spectral radius $\rho_\infty < 1.0$ is required to maintain numerical stability. However, this selection would result in a decrease of the total energy in the system . Consequently, a spectral radius of numerical damping of $\rho_\infty = 0.9$ was selected to provide the minimum numerical damping required to dissipate the spurious high frequency components, while minimizing the loss of the total energy. Finally, the finite element discretization of the beam results in a smallest modal period of $1/842.5 = 0.0012$ s. A stable time step needs to be about one-tenth of the smallest period [20]. Thus, the time integration step was set to 10^{-4} s for our finite element analysis.

The positions of the vibrating beam predicted by the finite element analysis are shown in Fig. 5 along with the experimental measurements. The finite element predictions and experimental measurements are in good agreement. Next, the predicted time histories of the tip displacements of the beam are shown in Fig. 6 with the experimentally measured displacements. Again, the finite element results agree with the experimental data very well.

5. Conclusion

In this work, we examined the dynamic characteristics of a new three-node curved beam element. The displacement interpolation functions of the curved beam element are based on a field consistency interpolation method and they satisfy the inextensible bending condition explicitly. Our effort shows that the resulting displacement interpolation functions will generate no membrane and torsional strains as expected except the flexural strain where the higher order non-zero terms approach zero at 4th order as the length of the element decreases. Accordingly, the displacement interpolation functions of the curved beam element satisfy the rigid body mode condition implicitly. In the case of a straight element, the displacement interpolation functions represent the rigid body terms explicitly and the error disappears. The numerical example of a free circular are shows that by using the implicit representation of the rigid body modes, it is possible to recover the rigid body modes, when the curved beam slenderness ratio is in the low to moderate range. The maximum error margin in these cases is 2.8%, even with a 180° (half-circular) element, In the example of a full circular ring, the accuracy in predicting the frequencies of non-rigid body modes was within 0.1%. The experimental work involving the vibration of a cantilever beam further demonstrated that the curved beam element is accurate and robust in analyzing this class of problems. It is concluded from the numerical and experimental works that the satisfaction of the rigid body mode condition implicitly in displacement interpolation functions of the curved beam element will not affect the accuracy and capability of the element in dynamic applications.

References

[1] D.G. Ashwell, A.B. Sabir, Limitations of certain curved finite elements when applied to arches, *International Journal of Mechanical Science* 13 (1971) 133–139.

[2] J.E.F. Guimaraes, G.R. Heppler, On trigonometric basis functions for CI curved beam finite elements, *Computers and Structures* 45 (1997) 405–413.

[3] D.J. Dawe, Some high-order elements for arches and shells, in: D.G. Ashwell, R.H. Gallagher (Eds.), *Finite Elements for Thin Shells and Curved Members*, Wiley, London, 1976, pp. 131–153.

[4] H.R. Meek, An accurate polynomial displacement function for finite elements, *Computers and Structures* 11 (1980) 265–269.

[5] J. Stolarski, T. Belytschko, Membrane locking and reduced integration for curved elements, *Journal of Applied Mechanics* 49 (1981) 172–178.

[6] G. Prathap, G.R. Bhashyam, Reduced integration and the shear flexible beam element, *International Journal for Numerical Methods in Engineering* 18 (1982) 195–210.

[7] G. Prathap, C.R. Babu, A linear thick curved beam element, *International Journal for Numerical Methods in Engineering* 23 (1986) 1313–1328.

[8] T.S. Balasubramanian, G. Prathap, A field consistent higher-order curved beam element for static and dynamic analysis of stepped arches, *Computers and Structures* 33 (1989) 281–288.

[9] P. Raveendranath, G. Singh, B. Pradhan, A two-noded locking-free shear flexible curved beam element, *International Journal for Numerical Methods in Engineering* 44 (1999) 265–280.

[10] P. Raveendranath, G. Singh, B. Pradhan, Free vibration of arches using a curved beam element based on a coupled polynomial displacement field, *Computers and Structures* 78 (2000) 583–590.

[11] P. Raveendranath, G. Singh, G.V. Rao, A three-noded shear-flexible curved beam element based on coupled displacement field interpolations, *International Journal for Numerical Methods in Engineering* 51 (2001) 85–101.

[12] M.X. Bucalem, K.J. Bathe, Locking behavior of isoparametric curved beam finite elements, *Applied Mechanics Review* 48 (1995) S25–S29.

[13] Z.H. Zhu, S.A. Meguid, Analysis of three-dimensional locking-free curved beam element, *International Journal of Computational Engineering Science* 5 (2004) 535–556.

[14] Z.H. Zhu, S.A. Meguid, Elastodynamic analysis of low tension cables using a new curved beam element, *International Journal of Solids and Structures* 43 (2006) 1492–1504.

[15] J.A. Stricklin, D.R. Navaratna, T.H.H. Pian, Improvements on the analysis of shells of revolution by the matrix displacement method, *AIAA Journal* 4 (1966) 2069–2072.

[16] S.S. Rao, *Mechanical Vibrations*, third ed., Addison-Wesley Publishing Company Inc., Reading, MA, 1995.

[17] R.D. Blevins, *Formulas forNatural Frequency and Mode Shape*, Van nostrand Reinhold Company, New York, 1979.

[18] T.J.R. Hughes, K.S. Pister, R.L. Taylor, Implicit-explicit finite elements in nonlinear transient analysis, *Computer Methods in Applied Mechanics and Engineering* 17/18 (1979) 159–182.

[19] D. Kuhl, M.A. Crisfield, Energy-conserving and decaying algorithms in non-linear structural dynamics, *International Journal for Numerical Methods in Engineering* 45 (1999) 569–599.

[20] K.J. Bathe, *Finite Element Procedures in Engineering Analysis*, Prentice-Hall, Englewood Cliffs, New Jersey, 1982.